Appendix A. Supplement to experimental set-up details

The present experiments were carried out in a return circuit low-speed wind tunnel of Beihang University, as shown in Figure 1 below. The cross-section of the wind tunnel test section was elliptical with a size of 1.02 m× 0.76 m at the inlet and 1.07 m×0.82 m at the outlet. The length of the test section was 1.45 m. The turbulence intensity is less than 0.3% for the maximum free stream velocity range of 50 m/s. At $\alpha = 31°$, i.e., the angle of attack mainly focused on in the present work, the blockage ratio due to the presence of the flying wing model is less than 2.86%.

The flying wing model used in the experiments was made of photosensitive resin material with a very smooth surface and the integrated processing was conducted through 3D printing technology. The tested model was mounted on a strut rod in the tail support manner, and then the strut rod was supported by two deep groove ball bearings. The model and the strut rod could roll together around the roll axis (*x*-axis) with a single degree of freedom. An electromagnetic lock was installed on the strut rod, which could lock the rod before the wind tunnel blew so that the model could not rotate freely. After the incoming wind velocity was stable, the electromagnetic lock would be released by following the command of the computer program, giving permission to the model and strut rod to roll freely from the release angle of $\phi_r = 0°$.

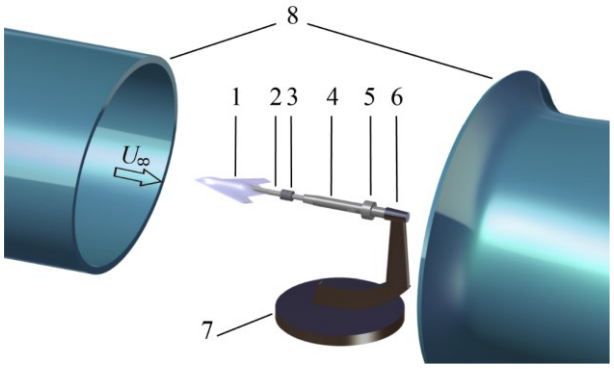

Figure 1. *Wind tunnel experimental device. 1: flying wing model, 2: strut rod, 3: coupling, 4: hermetic cavity, with bearing and electromagnetic lock installed inside it, 5: sensor bracket, with roll angle sensor installed inside it, 6: angle of attack mechanism, 7: base, 8: wind tunnel.*

Appendix B. Supplement to numerical set-up details

B.1. Grid sensitivity verification

Figure 2 shows the grid sensitivity verification of four different grids, G1, G2, G3, and G4, which had 9.6×10^6, 11.7×10^6, 14.1×10^6, and 18.4×10^6 cells, respectively. Here, the surface pressure coefficient on the leeward surface of $x = -0.5c$ cross-section was selected for comparison. The data at $\alpha = 10°$ was used for verification because of the violent variation of the surface pressure with time induced by the oscillation of the LEVs' breakdown location at $\alpha = 31°$ (as introduced in the Appendix E.1 below). The effect of the LEV's breakdown on the surface pressure is weak when $\alpha = 10°$. In Figure 2, the negative peak pressure in the range of $y/c = 0.3$ - 0.35 was induced by the LEV on the leeward surface. As can be seen, the difference between the results of different grids was mainly concentrated in this negative peak pressure region. However, with the increase in mesh density, the difference between the results of G3 and G4 had been small. Therefore, the G3 grid was finally selected for subsequent calculations. The numerical simulation of the 65° and 80° delta wings adopted a setting like that of the flying wing. The grids for 65° and 80° delta wings have 15.0×10^6 and 11.5×10^6 cells, respectively.

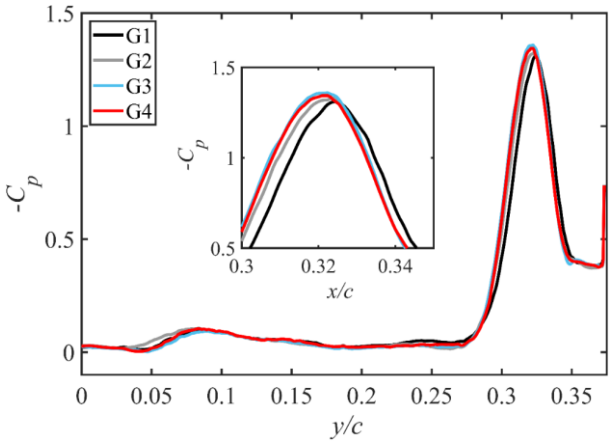

Figure 2. *Grid sensitivity verification by using the coefficient of pressure on the leeward surface of x = 0.8c cross section at* $\alpha = 10°$*. Due to the symmetry, only the region where y > 0 is shown in figure.*

B.2. Validation of numerical simulation

Figure 3 shows the comparison of roll angle time history of flying wing's wing rock obtained by wind tunnel experiment and numerical simulation under the condition of $U_\infty = 35\ \mathrm{m/s}$ and $\alpha = 31°$ (Case I). As can be seen that the trajectories of numerical simulation and experiment are qualitatively similar, though they do not completely coincide. This is because the wing rock of the flying wing is a highly complex nonlinear motion due to the coupling between the flow field evolution and the free motion of the model, where a slight disturbance will also have a great impact on the results. Even in wind tunnel experiments, repeated experiments under identical conditions cannot obtain the same trajectory. Therefore, to verify the effectiveness of numerical simulation results, it is necessary to quantitatively compare the statistics of roll angle history $\phi(t)$. There are three main statistics of $\phi(t)$: equilibrium roll angle position ϕ_0 (mean value), average oscillation amplitude ϕ_m (standard deviation), and oscillation frequency *f*. Table 2 shows the comparison of these three statistics of the experimental and numerical data. As can be seen that the numerical simulation results are very close to that of the experiment, and the error of all statistics is no more than 8.1%. The quantitative error between the experimental results and the numerical results can be attributed to these aspects: i) the model in the experiment has a strut rod, while the complete model is used in the numerical simulation without sting support interference; ii) the experimental result may be affected by the wind tunnel wall interference; iii) the bearing in the experiment has friction, but not in the numerical simulation. Therefore, as the influence of these factors, it can be considered that the difference between numerical simulation and experimental data is reasonable.

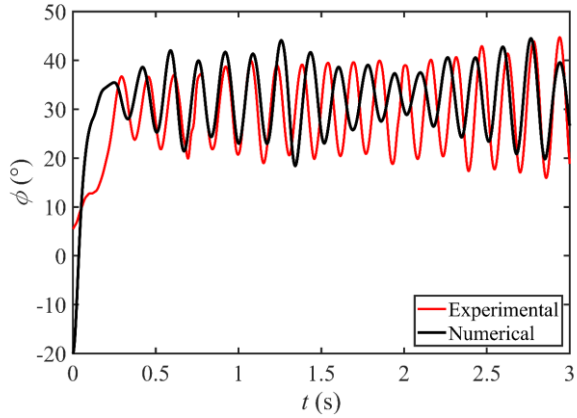

Figure 3. *Comparison of the roll angle time history in Case I obtained by experiment and numerical simulation.*

Table 2. *Comparison of statistics of experimental and numerical simulation data in Case I.*

Parameters	Experimental	Numerical	Relative error (%)
ϕ_0 (°)	30.08	32.07	6.6
ϕ_m(°)	7.26	6.67	8.1
f (Hz)	6.47	6.00	7.3

*Only the data in the range of t = 0.3s - 3s were counted.

Appendix C. Influence of angle of attack and freestream velocity on wing rock

Present wind tunnel experiments firstly focus on the influence of the angle of attack and freestream velocity motion to confirm the envelope of the flying wing's wing rock. Figure 4(a) shows the variation in the equilibrium roll angle ϕ_0 and average oscillation amplitude ϕ_m with the angle of attack. In Figure 4(a), there are two stages in which the oscillation amplitudes increase significantly: the first stage lasts from $\alpha = 28°$ to $\alpha = 33°$ and the second stage lasts from $\alpha = 44°$ to $\alpha = 46°$. However, the flying wing is found to have periodic self-induced oscillation only in the first stage. During the first stage, the periodic oscillation at $\alpha = 28°$ and $\alpha = 29°$ is unstable and intermittent, and the flying wing experiences continuous and stable wing rock only when $\alpha = 30°, 31°, 32°$, and $33°$. During the second stage, the flying wing oscillates non-periodically, experiencing the so-called wing drop phenomenon. Figure 4(b) shows the variation in the equilibrium roll angle ϕ_0 and average oscillation amplitude ϕ_m with freestream velocity U_∞ when $\alpha = 31°$. According to observation, all the cases in Figure 4(b) experience a periodic wing rock motion. Although the equilibrium roll angle ϕ_0 among the five cases changes slightly, the oscillation amplitude ϕ_m increases with the U_∞ before U_∞ = 35 m/s. However, the ϕ_m at U_∞ = 40 m/s has almost no obvious change compared with that at U_∞ = 35 m/s. This is speculated to be because the flying wing has already experienced the stable wing rock pattern after U_∞ = 35 m/s, and the system has reached a self-sustained form that tends to balance. Therefore, even though the freestream velocity keeps increasing, the roll system cannot continue to absorb more energy from the flow field and thus diverge.

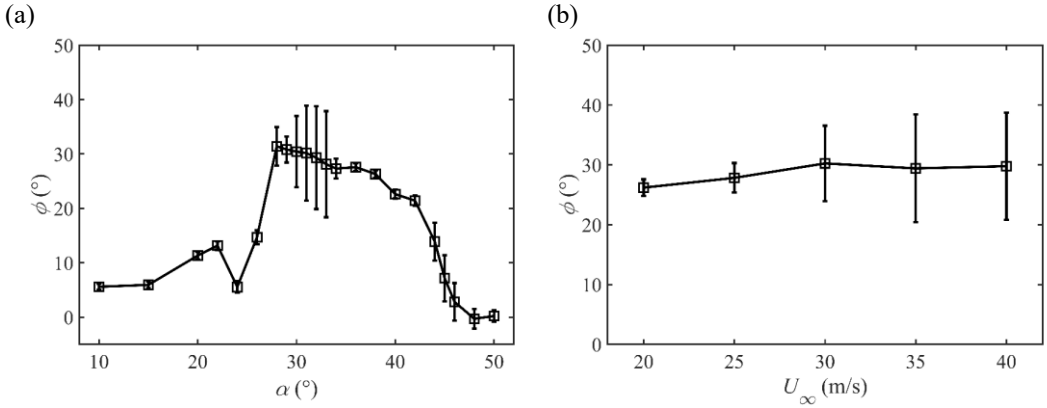

Figure 4. *Variation in the equilibrium roll angle ϕ_0 with (a) the angle of attack at $U_\infty = 35\ m/s$ and (b) the freestream velocity at $\alpha = 31°$. The vertical segments in the figure denote the mean oscillation amplitude ϕ_m.*

Appendix D. Physical meaning of hysteresis loop

Considering that the system composed of the flying wing model and strut rod is a rotation system with a single degree of freedom, if the friction of the bearing is neglected, the roll moment of the flow field acting on the model C_l can be calculated according to the rigid body dynamic equation

$$C_l(t) = I_x\ddot{\phi}(t)/(q_\infty Sb), \tag{1}$$

where C_l is the aerodynamic roll moment, q_∞ is the dynamic pressure of the freestream, and the meaning of I_x, S, and b has been introduced in the main manuscript. Arena & Nelson (1994) proposed that according to the energy exchange method of Nguyen, Yip, & Chambers (1981), the energy change of a single degree of freedom roll system is equal to the applied roll moment times the angular velocity and then integrated with respect to time. Therefore, the net energy absorbed or released by the roll system in a period can be expressed as

$$\Delta E = q_\infty S b \int_{t_1}^{t_2} C_l(t)\dot{\phi}(t)\mathrm{d}t. \tag{2}$$

Through a mathematical transformation, a more intuitive equation can be obtained:

$$\Delta E = q_\infty S b \int_{C_\phi} C_l\big(\phi(t)\big)\mathrm{d}\phi, \tag{3}$$

where C_ϕ is the curve formed by plotting the roll moment coefficient C_l as a function of the instantaneous roll angle $\phi(t)$. The physical explanation of this equation is as follows. In a wing rock motion cycle, the energy exchanged between the model and the flow field is directly related to the area surrounded by the $C_l - \phi$ curve. When the $C_l - \phi$ curve surrounds an area in a clockwise direction, energy is added to the roll system; conversely, when the $C_l - \phi$ curve surrounds an area in a counterclockwise direction, the energy of the roll system dissipates. For the strictly periodic wing rock motion, the area of the $C_l - \phi$ curve enclosed clockwise in a cycle must be equal to that enclosed counterclockwise to ensure the net energy balance of the roll system.

Appendix E. Static cases

Although the aircraft oscillates continuously and the flow field is highly unsteady during the wing rock motion, many previous studies have shown that wing rock dynamics depend on the aerodynamic characteristics in the static rolling (Jenkins, Myatt, & Hanff 1993; Katz 1999; Pelletier & Nelson 1998, 2000; Huang, Lou, & Hanff 2000; Nelson & Pelletier 2003), which includes but is not limited to the following aspects. Firstly, in some literature, the terminology “attractor” refers to the equilibrium position of free-to-roll motion. The attractors usually exist at the places where the static roll moment $C_l = 0$ and $\partial C_l/\partial\phi < 0$, i.e., the static roll moment determines the position and numbers of the attractors (which may exceed one in some cases). Furthermore, the oscillation amplitude can also be estimated from the distance between the attractor and the nearest critical state (Pelletier & Nelson 1998, 2000). On the other hand, the flow structures in the wing rock motion are usually like those in the static flow field but with more hysteretic characteristics. Comparison of the flow structures in a static flow field with that in a wing rock flow field is beneficial to understand the dynamic hysteresis effect in the wing rock motion (Arena & Nelson 1989; Arena 1992; Ng, Malcolm, & Lewis 1992). Therefore, the flow situation of the static flying wing, the 65° delta wing and the 80° delta wing at $\phi = 0°$ and $\phi = 30°$ are introduced below to establish a basic understanding of their aerodynamic loads and flow field characteristics. All the static cases in this section are implemented under the condition of $U_\infty = 35\ \mathrm{m/s}$ and $\alpha = 31°$, the same as dynamic cases.

E.1. Static cases with zero roll angle

Figure 5 shows the variation in roll moment coefficient C_l versus time for the static flying wing, the 65° delta wing and the 80° delta wing when the roll angle is kept at $\phi = 0°$. Figure 6 and Figure 7 show the corresponding contours of the surface pressure coefficient and Q = 750 isosurface of the flying wing and the delta wings at typical times, respectively. It can be seen from Figure 5 that for the flying wing and the 65° delta wing, although the model is symmetric when $\phi = 0°$, their roll moment oscillates violently. Analysis of the flow

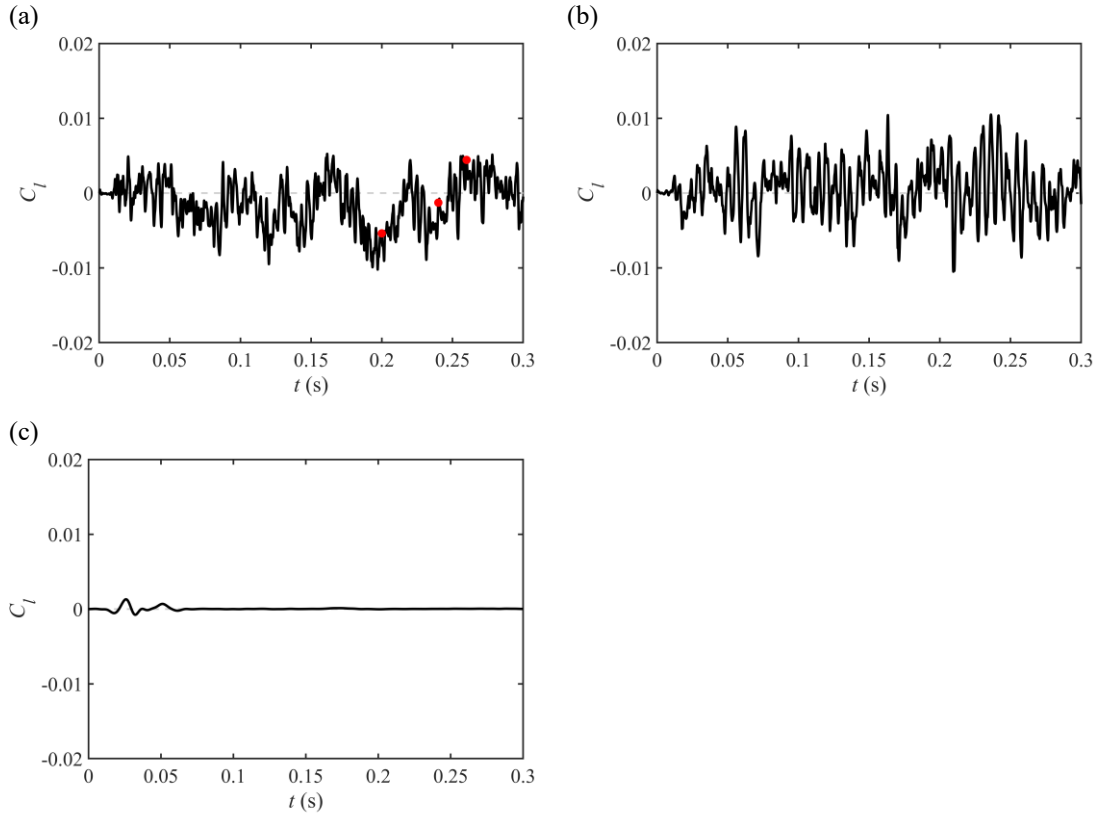

Figure 5. *Variation in roll moment coefficient versus time for the static (a) flying wing, (b) 65° delta wing and (c) 80° delta wing, with* $\phi = 0°$.

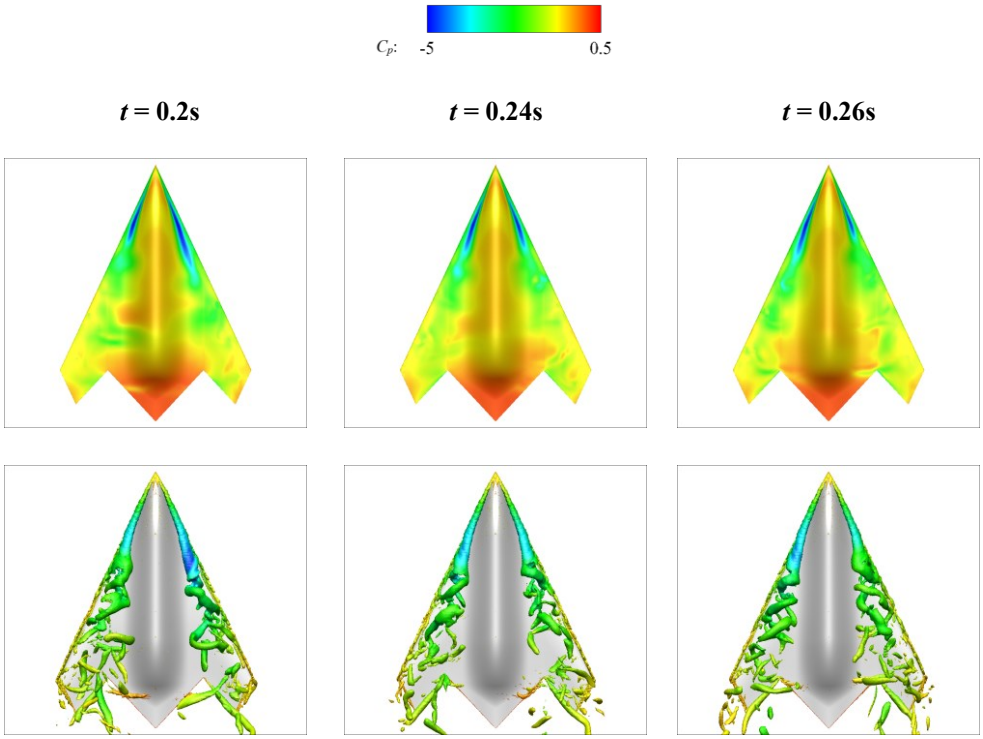

Figure 6. *Contour of surface pressure coefficient (first row) and Q = 750 isosurface coloured by* C_p *(second row) at three typical moments of t = 0.2s (first column), t = 0.24s (second column), and t = 0.26s (third column) in Case Static 1, with* $\phi = 0°$.

structures shows that this oscillation is due to the LEVs' breakdown points of the flying wing and the 65° delta wing having developed upstream of the trailing edge when $\alpha = 31°$ and the severe oscillation of the vortex breakdown points along the streamwise causes an unsteady surface pressure on the leeward side. In the previous studies on delta wings, the oscillation of the LEV's breakdown points along the streamwise is common and has received extensive attention. When this phenomenon occurs, the streamwise breakdown locations of the bilateral leading-edge vortices experience an antisymmetric quasi-periodic dynamic fluctuation (Delery 1994; Gursul & Yang 1995; Menke, Yang & Gursul 1999; Gursul 2005; Shen & Wen 2018). Figure 6 shows the flow field of the flying wing at three typical moments of t = 0.2s, t = 0.24s, and t = 0.26s, marked with red dots in Figure 5(a). It can be seen from Figure 6 that at t = 0.2s, the breakdown point of the left-hand side LEV is closer to the apex of the flying wing than that of the right-hand side LEV. Therefore, the right-hand side LEV induces a larger negative pressure region on the leeward surface, corresponding to a negative roll moment in Figure 5(a). At t = 0.24s, the locations of the breakdown points of two LEVs, as well as their induced surface pressure, are not significantly different, corresponding to a roll moment with a small absolute value. At t = 0.26s, the streamwise breakdown locations of the left-hand side and right-hand side LEVs reversed compared to that at t = 0.2s, inducing a stronger negative pressure on the left-hand side surface, corresponding to a positive roll moment. The oscillation of the roll moment explains the experimental phenomenon that the flying wing rolls left or right randomly after being released from $\phi_r = 0°$, which is also the reason for all models being released from $\phi_r = -20°$ rather than $\phi_r = 0°$ in the numerical simulation. Besides, since the LEVs' breakdown location of the 65° delta wing is close to that of the flying wing (Figure 7), there is also a fluctuation oscillation of its LEVs' breakdown points, which will also cause the oscillation of the roll moment coefficient. In contrast, the roll moment of the 80° delta wing remains around 0 without oscillation after calculation convergence, which is attributed to that the LEVs' breakdown points of the 80° delta wing do not develop to the upstream of the trailing edge at $\alpha = 31°$, and therefore the LEVs' breakdown has nearly no effect on the surface pressure (Figure 7).

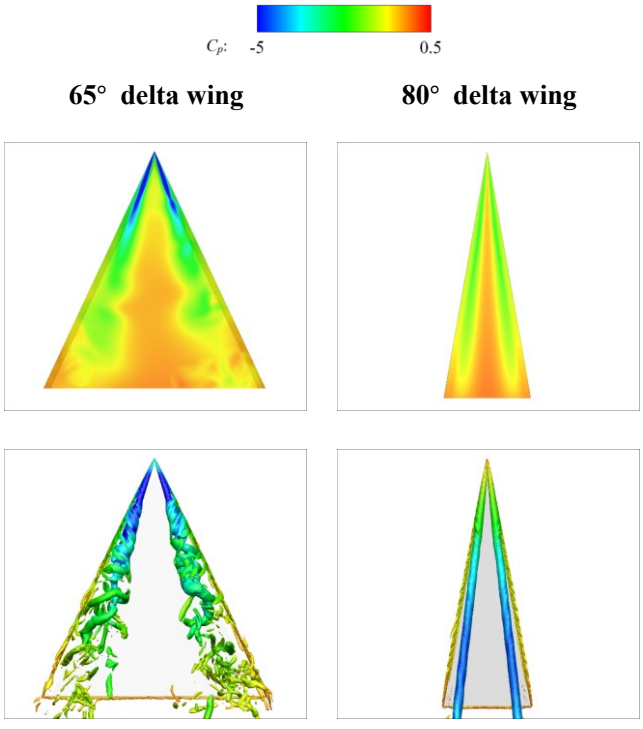

Figure 7. *Contour of surface pressure coefficient (first row) and Q = 750 isosurface coloured by C_p (second row) at a typical moment in Case Static 3 and Case Static 5, with* $\phi = 0°$.

Besides the streamwise location of the vortex breakdown, the vortex strength, and the spanwise and normal position of the LEV's core are also important factors affecting the surface pressure induced by the vortex. For the sake of simplification, the above analysis did not fully consider these factors. However, variations in the strength of the LEV and the position of its vortex core have also been observed in the present research. The mechanism explanation for these LEV-related unsteady flow phenomena is complex and may be related to the crossflow instability or interference between vortices. As this is not the topic of the present research, interested readers can follow more research (Gursul, Gordnier, & Visbal 2005; Breitsamter 2008; Ma, Wang, & Gursul 2017; Eldredge & Jones 2019).

E.2. Static cases with high roll angle

As can be seen from Figures 6 and 7, when $\phi = 0°$, the flying wing, 65° delta wing, and 80° delta wing all have bilateral LEVs. However, the situation is different under high roll angles. The conditions of all cases in Figure 8 are the same as those in Figures 6 and 7, except for the roll angle of all models is $\phi = 30°$. The roll angle of $\phi = 30°$ is selected for display because this location is close to the equilibrium roll angle ϕ_0 in the wing rock

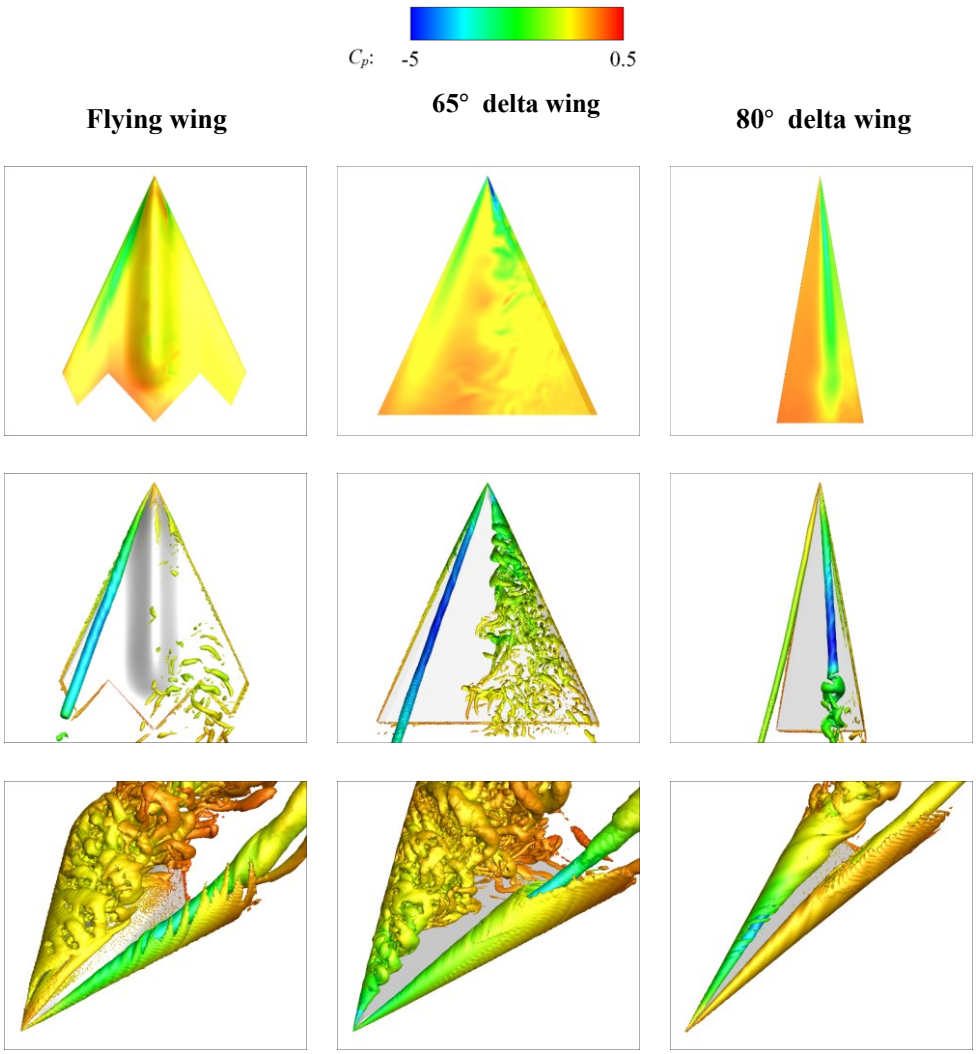

Figure 8. *Contour of surface pressure coefficient (first row), Q = 750 isosurface coloured by C_p (second row) and Q = 15 isosurface colored by C_p (third row) at a typical moment in Case Static 2, Case Static 4, and Case Static 6, with* $\phi = 30°$.

case of the flying wing (Case I). In addition, the axonometric views of the Q = 15 isosurface are supplemented in Figure 8 to show the relevant flow structures more clearly. It can be seen from Figure 8 that although the flow field of the 65° delta wing and 80° delta wing is asymmetry they still have bilateral LEVs. Although the breakdown location of the right-hand side (sinking side) LEV of the 65° delta wing is very close to the apex due to the influence of the effective angle of attack, this LEV still induces a strong negative pressure area on the wing surface. However, no LEV is formed on the right-hand side (sinking side) of the flying wing due to its specific nose geometry. The right-hand side shear layer separates from the leading edge of the flying wing, exists in the form of a vorticity layer, and then transits into turbulent structures. In the range where the right-hand side shear layer exists, no concentrated strong negative pressure is induced on the wing surface. The unique "vortex-shear-layer" structure of the flying wing is significantly different from the "vortex-vortex" structure of the delta wing, which is also one of the unique flow foundations of the flying wing's wing rock.

Appendix F. Frequency spectrum and hysteresis loop of numerically simulated roll angle

Figure 9 shows the frequency spectrum of roll angle $\phi(t)$ and $C_l - \phi$ hysteresis loop for the flying wing and the 80° delta wing. The $C_l - \phi$ hysteresis loop of the flying wing in Figure 9(b) is the phase-averaged result of the data in Figure 3(a) of the main manuscript, with the data after t = 0.3 s being used. As the 80° delta wing has a good periodicity in the steady stage, the situation in each cycle is similar, Figure 9(d) gives the $C_l - \phi$ hysteresis loop of one steady-state cycle (from time A to E). It can be confirmed from Figures 9(a) and (b) that, for the flying wing's wing rock motion, the second harmonic component of the roll angle $\phi(t)$ is the second-dominant frequency, and the $C_l - \phi$ hysteresis loop is in the bicyclic form, which is entirely consistent with

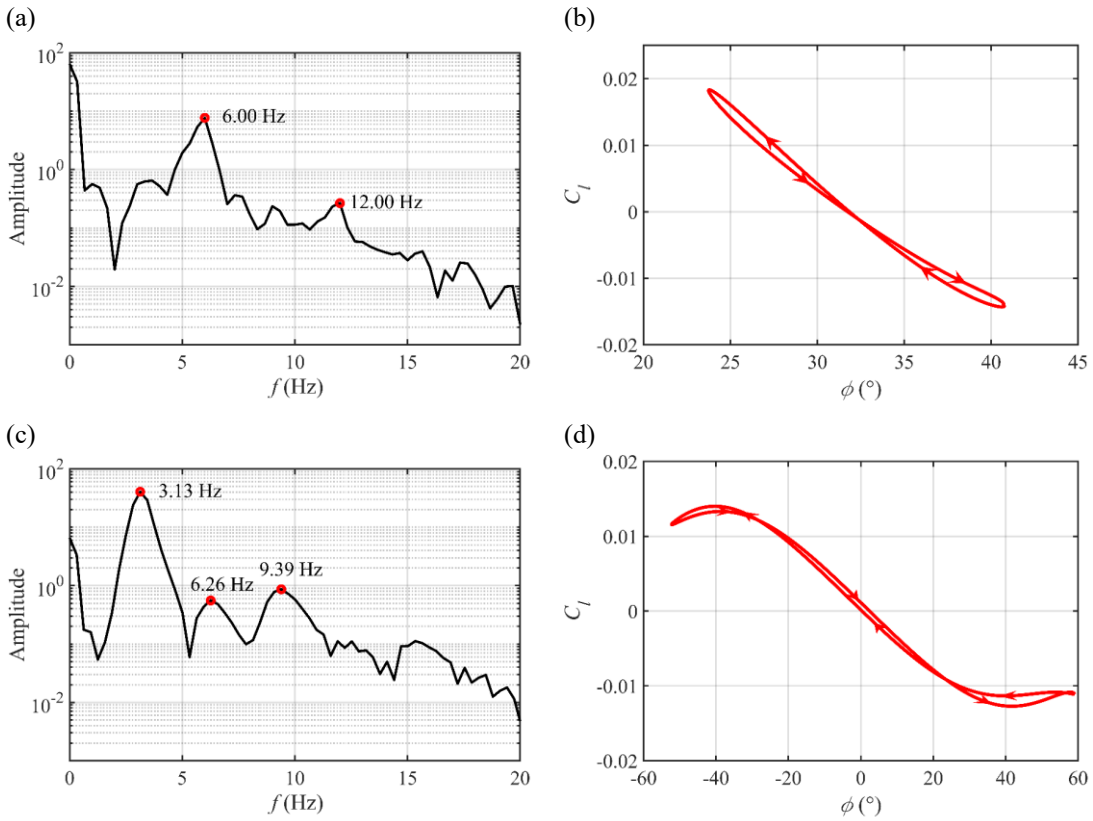

Figure 9. *(a) Frequency spectrum of the roll angle $\phi(t)$ in Case I, (b) phase-averaged $C_l - \phi$ hysteresis loop in Case I, (c) frequency spectrum of the roll angle $\phi(t)$ in Case III, (d) instantaneous $C_l - \phi$ hysteresis loop in Case III.*

present experimental results. In contrast, the frequency spectrum of the roll angle $\phi(t)$ of the 80° delta wing has a dominant frequency, a second, and a third harmonic component. Moreover, the peak value of the third harmonic component is higher than that of the second harmonic component (Figure 9(c)). Accordingly, the 80° delta wing's hysteresis loop is also in the tricyclic form (Figure 9(d)), being consistent with the previous experimental results (Arena & Nelson 1994; Nelson & Pelletier 2003).

Appendix G. Streamlines of different aircraft

To further compare the difference in flow structures between the flying wing and the delta wings, Figure 10 shows partial streamlines in the flow field of these aircraft, colored by *x*-vorticity. All the aircraft in Figure 10 are around their equilibrium position of free-to-roll motion, respectively. In these figures, the streamlines contained in the LEV and separated from the leading edge are specially selected. As can be seen, the streamlines separating from the right-hand side leading edge of the flying wing do not curl, but instead, cross the bulge on the leeward surface of the fuselage and finally close to the left-hand side LEV, reflecting the influence of sideslip under high roll angles. In the flow field of the 65° and 80° delta wings, the streamlines separated from the leading edges are curled into the LEVs. The difference is that the LEVs of the 80° delta wing remain complete until near the trailing edge, while the LEVs of the 65° delta wing burst above the middle of the wing.

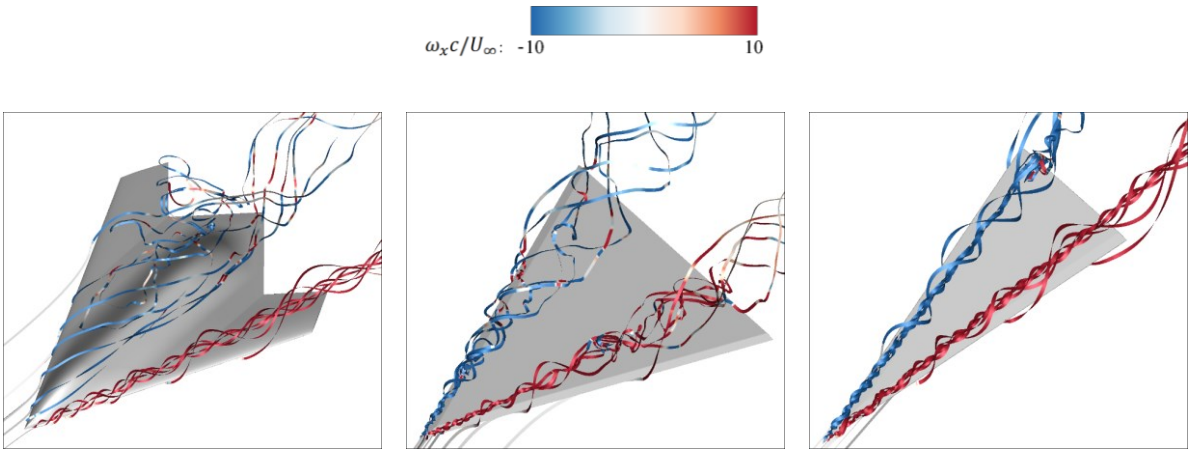

Figure 10. *Partial streamlines in the flow field of the flying wing (left), the 65° delta wing (middle), and the 80° delta wing (right). The streamlines are colored by x-vorticity. The flow field of the flying wing and the 80° delta wing is selected at moment B, and the flow field of the 65° delta wing is selected at t = 1s.*

Appendix H. Definition of LEV-related physical quantities

Figures 11(a) and (b) show the *x*-vorticity contours on three different *x*-sections (x = -0.3c, x = -0.5c and x = -0.8c) of the flying wing and the 80° delta wing at time B, respectively. As can be seen from Figure 11(a), the left-hand side LEV of the flying wing has an integral shape, but the right-hand side shear layer is dispersed, so it is difficult to accurately identify the boundary of the shear layer through the common vortex identification methods. Therefore, according to the observation of the current results, a normal vertical line y = -0.25b_x is selected as the boundary to split the LEV and the shear layer (as shown by the vertical dotted line in Figure 11(a)). All the negative vorticity on the right-hand side of the boundary, i.e., in the range of y > -0.25b_x is taken as an integral part of the shear layer. Here, b_x is the local wingspan at the *x*-section. According to this standard, the total circulation of the shear layer is defined as

$$\Gamma^- = \iint_{\Delta^-} \omega_x d\delta = \int_{y>-0.25b_x}^{+\infty} \int_{-z>-z_{lee}}^{-\infty} \omega_x^- \, \mathrm{d}z\mathrm{d}y. \tag{4}$$

Here, Δ^- is the integral region, including the area on the right of the boundary line $y = -0.25b_x$ above the leeward surface, z_{lee} is the z-coordinate of the leeward surface profile, and ω_x^- is the negative vorticity. Correspondingly, the normal position and spanwise position of the vorticity centroid of the shear layer are defined as

$$z^- = \frac{1}{\Gamma^-} \iint_{\Delta^-} z\omega_x^- d\delta, \tag{5}$$

$$y^- = \frac{1}{\Gamma^-} \iint_{\Delta^-} y\omega_x^- d\delta. \tag{6}$$

Although the boundary of the left-hand side LEV of the flying wing can be identified by various vortex identification methods, to be consistent with the calculation method of the right-hand side shear layer, the positive vorticity in the range of $y < -0.25b_x$, including the vorticity in the LEV and the left-hand side shear layer connected with the LEV, is used to calculate the total circulation

$$\Gamma^+ = \iint_{\Delta^+} \omega_x d\delta = \int_{y<-0.25b_x}^{+\infty} \int_{-z>-z_{lee}}^{-\infty} \omega_x^+ \, \mathrm{d}z\mathrm{d}y, \tag{7}$$

the normal position and spanwise position of the vorticity centroid

$$z^+ = \frac{1}{\Gamma^+} \iint_{\Delta^+} z\omega_x^+ d\delta, \tag{8}$$

$$y^+ = \frac{1}{\Gamma^+} \iint_{\Delta^+} y\omega_x^+ d\delta, \tag{9}$$

where Δ^+ is the integral region and ω_x^+ is the positive vorticity in Δ^+. To compare with the flying wing, the calculation of the total circulation and vorticity centroid position for the 80° delta wing adopts the same method as that of the flying wing, except that the vertical line $y = 0$ is selected as the splitting boundary (the vertical dotted line shown in Figure 11(b)). In Figures 11(a) and (b), the identification result of the vorticity centroid based on the above method is marked with black dots.

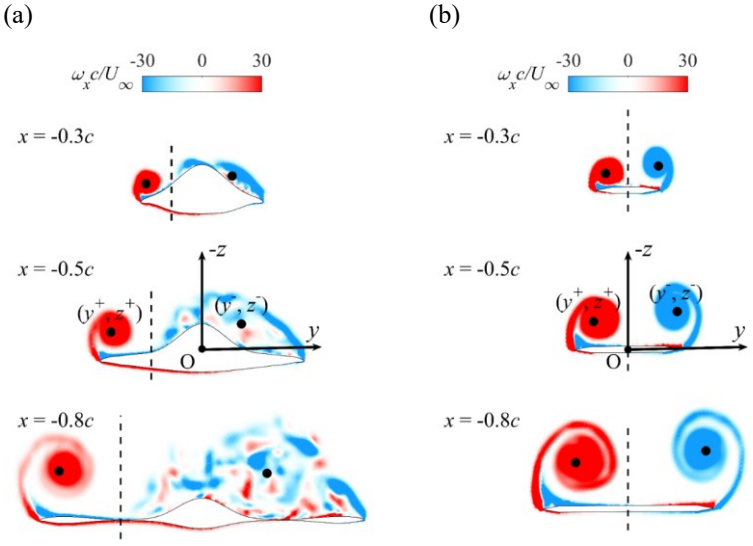

Figure 11. *Vorticity contours on different sections at time B in (a) Case I and (b) Case III.*

Appendix I. Discussion

The above research shows that the flying wing with a 65° sweep angle can experience periodic self-induced oscillation under certain conditions, but the 65° delta wing cannot. Why there is a significant difference in the free-to-roll characteristics of two aircraft with the same aspect ratio is a question that needs to be carefully examined. According to our knowledge, both slender and non-slender delta wings can experience periodic wing rock oscillation. Among them, the wing rock of the slender delta wing is widely known, and the delta wing with a sweep angle of $\Lambda \geq 75°$ has been reported to have periodic self-induced oscillation (Levin & Katz 1984; Ng, Malcolm & Lewis 1989, 1992; Lee & Batina 1991; Ericsson 1993; Arena & Nelson 1994). Low roll damping is closely related to the cause of wing rock of the slender delta wings (Ericsson & King 1992; Ericsson 1993). The equilibrium roll angle position of the slender delta wing's wing rock is usually around 0° (Gursul 2005). A possible mechanism to sustain this kind of wing rock motion is the hysteresis in the location and strength of the LEVs (Arena & Nelson 1994). The non-slender delta wing, with a sweep angle of $\Lambda \leq 60°$, can also experience periodic wing rock. The delta wing with a sweep angle equal to 45°, 50°, 55°, and 60° has been found to have self-induced oscillation in previous experiments (Ueno, Matsuno, & Nakamura 1998; Matsuno & Nakamura 2000; Ericsson 2001; Matsuno, Yokouchi, & Nakamura 2000, 2003; McClain et al. 2007; Gresham, Wang, & Gursul 2010). These delta wings usually have a non-zero oscillation equilibrium position, which implies a more complex flow mechanism (Gursul, Gordnier, & Visbal 2005). Besides the above slender and non-slender delta wings, the transitional models between these two types, such as the delta wing with a sweep angle of 65° and 70°, are found to have no self-induced oscillation (Ng, Malcolm, & Lewis 1992; Gresham, Wang, & Gursul 2010), which is a very interesting phenomenon. Due to its fascinating dynamics characteristics, many previous studies (Hanff & Jenkins 1990; Jenkins, Myatt, & Hanff 1993; Ericsson & Hanff 1994; Pamadi, Rao, & Vigyan 1994; Chaderjian & Schiff 1994, 1996; Ericsson 1995a, b; Huang & Hanff 1999; Huang, Lou, & Hanff 2000, 2002) focused on the free-to-roll motion of the 65° delta wing and found that it has multiple equilibrium positions, i.e., multi-attractors phenomenon. Moreover, the equilibrium position of the 65° delta wing also has bifurcation behaviors (Huang, Lou, & Hanff 2000). However, due to the complexity of the dynamics related to the 65° delta wing, we have not found a perfect explanation for why the 65° delta wing cannot have periodic self-induced oscillation.

The flying wing in this study also has a sweep angle of 65°, but it can undergo periodic wing rock oscillations. This comparison indicates that although the sweep angle or slenderness is an important factor affecting roll damping, it is not the only one. If modifying the 65° delta wing to be a double-delta wing (Pelletier & Nelson 1998; Yoshinaga, Otaka, & Tate 2001), the double-delta wing can experience periodic wing rock again, which indicates the flow near the nose of the delta wing is essential to the self-excited oscillation. According to the present analysis, the camber bulge near the nose of the flying wing occupies the space originally belonging to the LEV, making it impossible to form a complete LEV on the sinking side like the 65° delta wing, while the pressure hysteresis caused by the variation of the uplifting-side LEV is speculated to be an essential mechanism in maintaining the periodic wing rock oscillation. Therefore, the specific sweep angle and fuselage shape result in a special flow structure, which is necessary for the flying wing's wing rock oscillation. Present results inspire the design of future flying wing configuration, that is, the leeward-side fuselage profile, especially near the nose, needs to be carefully designed as it may be a crucial factor affecting lateral stability.

References

Arena, A. S. An experimental and computational investigation of slender wings undergoing wing rock. PhD dissertation, University of Notre Dame, April 1992.

Arena, A. S., & R. C. Nelson. “The Effect of Asymmetric Vortex Wake Characteristics on a Slender Delta Wing Undergoing Wing Rock Motion.” AIAA Paper, 1989-3348, 1989.

Arena, A. S., & Nelson, R. C. “Experimental Investigations on Limit Cycle Wing Rock of Slender Wings.” Journal of Aircraft, Vol. 31, No. 5, 1994, pp. 1148–1155.

Breitsamter, C. “Unsteady Flow Phenomena Associated with Leading-Edge Vortices.” Progress in Aerospace Sciences, Vol. 44, 2008, pp. 48–65.

Chaderjian, N. M., & Schiff, L. B. “Navier-Stokes Prediction of Large-Amplitude Forced and Free-to-Roll Delta-Wing Oscillations.” AIAA Paper 1994-1884, 1994.

Chaderjian, N. M., & Schiff, L. B. “Numerical Simulation of Forced and Free-to-Roll Delta-Wing Motions.” Journal of Aircraft, Vol. 33, No. 1, 1996, pp. 93–99.

Delery, J. M. “Aspects of Vortex Breakdown.” Progress in Aerospace Sciences, Vol. 30, No. 1, 1994, pp. 1–59.

Eldredge, J. D., and Jones, A. R. “Leading-Edge Vortices: Mechanics and Modeling.” Annual Review of Fluid Mechanics, Vol. 51, 2019, pp. 75–104.

Ericsson, L. E. “Slender Wing Rock Revisited.” Journal of Aircraft, Vol. 30, No. 3, 1993, pp. 352–356.

Ericsson, L. E. “Flow Physics of Critical States for Rolling Delta Wings.” Journal of Aircraft, Vol. 32, No. 3, 1995a, pp. 603–610.

Ericsson, L. E. “Wing Rock Analysis of Slender Delta Wings, Review and Extension.” Journal of Aircraft, Vol. 32, No. 6, 1995b, pp. 1221–1226.

Ericsson, L. E. “Wing Rock of Nonslender Delta Wings.” Journal of Aircraft, Vol. 38, No. 4, 2001, pp. 784–784.

Ericsson, L. E., & Hanff, E. S. “Further Analysis of High-Rate Rolling Experiments of a 65-Deg Delta Wing.” Journal of Aircraft, Vol. 31, No. 6, 1994, pp. 1350–1357.

Ericsson, L. E., & King, H. H. C. “Rapid Prediction of High-Alpha Unsteady Aerodynamics of Slender-Wing Aircraft.” Journal of Aircraft, Vol. 29, No. 1, 1992, pp. 85–92.

Gresham, N. T., Wang, Z., & Gursul, I. “Vortex Dynamics of Free-to-Roll Slender and Nonslender Delta Wings.” Journal of Aircraft. Vol., 47, 2010, pp. 292–302.

Gursul, I., Gordnier, R., & Visbal, M. “Unsteady Aerodynamics of Nonslender Delta Wings.” Progress in Aerospace Sciences, Vol. 41, No. 7, 2005, pp. 515–557.

Gursul, I., & Yang, H., “On Fluctuations of Vortex Breakdown Location,” Physics of Fluids, Vol. 7, No. 1, 1995, pp. 229–231

Gursul, I. “Review of Unsteady Vortex Flows over Slender Delta Wings,” Journal of Aircraft, Vol. 42, No. 2, 2005, pp. 299–319.

Hanff, E. S., & Jenkins, S. B. “Large-Amplitude High-Rate Roll Experiments on a Delta and Double Delta Wing.” AIAA Paper 1990-0224, 1990.

Huang, X. Z., & Hanff, E., S. “Free-to-Roll Trajectory and Related Attractors of a 65° Delta Wing Rolling at High Incidence.” AIAA Paper 1999-4103, 1999.

Huang, X. Z., Lou, H. Y., & Hanff, E. S. “Bifurcation Analysis of a 65° Delta Wing Rolling at High Incidence.” AIAA Paper 2000-3911, 2000.

Huang, X. Z., Lou, H. Y., & Hanff, E. S. “Non-Linear Indicial Response and Internal State-Space Representation for Free-to-Roll Trajectory Prediction of a 65° Delta Wing at High Incidence.” AIAA Paper 2002-4713, 2002.

Jenkins, J. E., Myatt, J. H., & Hanff, E. S. “Body-Axis Rolling Motion Critical States of a 65-Degree Delta Wing,” AIAA Paper 1993-0621, 1993.

Katz, J. “Wing/Vortex Interactions and Wing Rock,” Progress in Aerospace Sciences, Vol. 35, No. 7, 1999, pp. 727–750.

Lee, E. M., & Batina, J. T. “Conical Euler methodology for unsteady vortical flows about rolling delta wings.” AIAA Paper 1991-0730, 1991.

Levin, D., & Katz, J. “Dynamic Load Measurements with Delta Wings Undergoing Self-Induced Roll Oscillations.” Journal of Aircraft, Vol. 21, No. 1, 1984, pp. 30–36.

Ma, B.-F., Wang, Z., and Gursul, I. “Symmetry Breaking and Instabilities of Conical Vortex Pairs over Slender Delta Wings.” Journal of

Fluid Mechanics, Vol. 832, 2017, pp. 41 – 72.

Matsuno, T., & Nakamura, Y. “Self-Induced Roll Oscillation of 45-Degree Delta Wings.” AIAA Paper 2000-0655, 2000.

Matsuno, T., Yokouchi, S., & Nakamura, Y. “The Effect of Leading-Edge Profile on Self-Induced Oscillation of 45-Degree Delta Wings.” AIAA Paper 2000-4004, 2000.

Matsuno, T., Yokouchi, S., & Nakamura, Y. “Data-Based Modeling of Non-Slender Wing Rock.” AIAA Paper 2003-738, 2003.

McClain, A., Wang, Z., Vardaki, E., & Gursul, I. “Unsteady Aerodynamics of Free-to-Roll Nonslender Delta Wings.” AIAA Paper, 2007-1074, 2007.

Menke, M., Yang, H., & Gursul, I., “Experiments on the Unsteady Nature of Vortex Breakdown over Delta Wings,” Experiments in Fluids, Vol. 27, No. 3, 1999, pp. 262 – 272.

Nelson, R. C., & Pelletier, A. “The Unsteady Aerodynamics of Slender Wings and Aircraft Undergoing Large Amplitude Maneuvers,” Progress in Aerospace Sciences, Vol. 39, 2003, pp. 185 – 248.

Ng, T. T., Malcolm, G. N., & Lewis, L. C. “Flow Visualization Study of Delta Wings in Wing-Rock Motion.” AIAA Paper, 1989-2187, 1989.

Ng, T. T., Malcolm, G. N., & Lewis, L. C. “Experimental Study of Vortex Flows over Delta Wings in Wing-Rock Motion.” Journal of Aircraft, Vol. 29, No. 4, 1992, pp. 598 – 603.

Nguyen, L. T., Yip, L., & Chambers, J. R. “Self-Induced Wing Rock of Slender Delta Wings.” AIAA Paper 1981-1883, 1981.

Pamadi, B. N., Rao, D. M., & Vigyan, Y. N. “Wing Rock and Roll Attractor of Delta Wings at High Angles of Attack.” AIAA Paper 1994-0807, 1994.

Pelletier, A., & Nelson, R. C. “Dynamic Behavior of an 80°/65° Double-Delta Wing in Roll.” AIAA Paper, 1998-4353, 1998.

Pelletier, A., & Nelson, R. C. “The Importance of Critical States in Nonlinear Aerodynamics.” AIAA Paper, 2000-3909, 2000.

Shen, L., & Wen C., -Y. “Oscillations of Leading-Edge Vortex Breakdown Locations over a Delta Wing.” AIAA Journal, Vol. 56, No. 6, 2018, pp. 2113 – 2118.

Ueno, M., Matsuno, T., & Nakamura, Y. “Unsteady Aerodynamics of Rolling Thick Delta Wing with High Aspect Ratio.” AIAA Paper 1998-2520, pp. 226 – 234, 1998.

Yoshinaga, T., Otaka, S., & Tate, A. “Wing Rock of Double Delta Wings.” AIAA Paper 2001-4078, 2001.